

Rate constants for the formation of SiO by radiative association

M. Cairnie,¹ R. C. Forrey,^{1★} J. F. Babb,^{2★} P. C. Stancil³ and B. M. McLaughlin^{2,4★}

¹*Department of Physics, Penn State University, Berks Campus, Reading, PA 19610-6009, USA*

²*Institute for Theoretical Atomic, Molecular and Optical Physics (ITAMP), Harvard-Smithsonian Center for Astrophysics, 60 Garden St., Cambridge, MA 02138, USA*

³*Department of Physics and Astronomy and the Center for Simulation Physics, University of Georgia, Athens, Georgia 30602, USA*

⁴*Centre for Theoretical Atomic Molecular and Optical Physics (CTAMOP), School of Mathematics and Physics, Queens University Belfast, Belfast BT7 1NN, UK*

Accepted 2017 July 5. Received 2017 June 27; in original form 2017 May 15

ABSTRACT

Accurate molecular data for the low-lying states of SiO are computed and used to calculate rate constants for radiative association (RA) of Si and O. Einstein A-coefficients are also calculated for transitions between all of the bound and quasi-bound levels for each molecular state. The radiative widths are used together with elastic tunnelling widths to define effective RA rate constants which include both direct and indirect (inverse pre-dissociation) formation processes. The indirect process is evaluated for two kinetic models which represent limiting cases for astrophysical environments. The first case scenario assumes an equilibrium distribution of quasi-bound states and would be applicable whenever collisional and/or radiative excitation mechanisms are able to maintain the population. The second case scenario assumes that no excitation mechanisms are available which corresponds to the limit of zero radiation temperature and zero atomic density. Rate constants for SiO formation in realistic astrophysical environments would presumably lie between these two limiting cases.

Key words: astrochemistry – molecular data – molecular processes – scattering – ISM: molecules.

1 INTRODUCTION

The formation of dust in environments such as the inner winds of AGB stars (Cherchneff 2006), the ejecta of novae (Rawlings & Williams 1989) and the ejecta of supernovae (Lepp, Dalgarno & McCray 1990) depends on the production of molecules, either as precursors of dust grains or as competitors to dust production.

The formation of CO and SiO in such environments can be modelled using large networks of chemical reactions, which depend on the knowledge of rate constants for individual chemical reactions relating to the molecule species. For example, these models have been applied in explaining the observations of CO (Lepp et al. 1990; Gearhart, Wheeler & Swartz 1999) and SiO (Liu & Dalgarno 1996) in the ejecta of Supernova 1987A, the inner winds of AGB stars (Willacy & Cherchneff 1998), and the outer envelopes of carbon-rich (Cherchneff 2012; Li et al. 2014) and oxygen-rich (Li et al. 2016) stars. In fact, the observation of SiO in carbon-rich stars suggests a shock-induced chemistry which dissociates CO freeing up atomic oxygen to form SiO and other oxides (Cherchneff 2012).

While in typical interstellar medium environments, SiO is formed primarily by the exchange reaction



the radiative association (RA) process may become competitive, particularly in hydrogen-deficient gas. For applications to various astrophysical environments, RA was studied for CO (Dalgarno, Du & You 1990; Franz, Gustafsson & Nyman 2011; Antipov, Gustafsson & Nyman 2013) and for SiO (Andreazza, Singh & Sanzovo 1995; Forrey et al. 2016).

The RA process for SiO formation is believed to be a key step in the subsequent formation of silicates and dust (Marassi et al. 2015). Therefore, it is of considerable interest to provide a comprehensive set of reliable rate constants for all contributions to the RA processes



and



where $h\nu$ represents an emitted photon. Here, the $\text{Si} \cdots \text{O}$ metastable state in (3) may be formed as an intermediate step in process (2) or by an independent process such as inverse predissociation.

In a recent publication (Forrey et al. 2016), here referred to as Paper I, our group performed detailed quantum chemistry calculations to obtain potential energy curves (PEC's) and transition dipole moments (TDM's) for the low-lying molecular states of SiO. We then used the high quality molecular data for the $X^1\Sigma^+$ and $A^1\Pi$ states, and the TDM coupling the states, to obtain rate constants for RA of $\text{Si}(^3P)$ and $\text{O}(^3P)$ via approach on the $A^1\Pi$ molecular curve.

* E-mail: rcf6@psu.edu (RCF); jbabb@cfa.harvard.edu (JFB); bmclaughlin899@btinternet.com (BMMc)

We found that the direct rate constants were roughly a factor of 10 smaller than those calculated earlier by Andreazza et al. (1995).

In this work, we extend our initial calculations reported in Paper I to include SiO formation by RA via approach on the $E^1\Sigma^+$, $2^1\Pi$, $3^1\Pi$ and $D^1\Delta$ molecular states. In addition to computing the direct RA contribution (2) for each intermediate electronic state, we also calculate tunnelling and radiative lifetimes for all of the quasi-bound vibrational states in order to provide estimates of the indirect resonant contribution (3) for different kinetic conditions.

In Paper I, we showed that resonances may play an important role in enhancing the rate constants for the formation of SiO. With the assumption that all quasi-bound levels were in local thermodynamic equilibrium (LTE), we obtained rate constants for low temperatures which were several orders of magnitude larger than those predicted by standard quantum scattering formulations. The RA rate constants were defined to include both direct and indirect (inverse predissociation) formation processes. The direct contribution was computed using semiclassical (Bates 1951) and quantum mechanical methods (Zygelman & Dalgarno 1990; Stancil, Babb & Dalgarno 1993; Nyman, Gustafsson & Antipov 2015; Forrey et al. 2016; Öström et al. 2016) and excellent agreement was achieved. The indirect contribution relied on the kinetic LTE assumption for the quasi-bound levels, which would be applicable whenever collisional and/or radiative excitation mechanisms are able to maintain an equilibrium population. For low-density environments which are not subjected to substantial radiation, the indirect contribution would clearly be less than the LTE result.

We now consider two rate constants which we believe represent limiting cases for RA. The first rate constant is the LTE rate constant described above. The second rate constant, referred to as the NLTE rate constant in the zero-density limit (ZDL), considers the indirect formation process for a non-LTE environment which has zero radiation temperature and an atomic density $n \ll n_{\text{cr}}$, where n_{cr} is the critical density determined by equating the efficiency of RA with that of three-body recombination (TBR). With this definition, the NLTE-ZDL rate constant is equivalent to conventional methods that include radiative broadening in the resonance contribution when the tunnelling width is smaller than or comparable to the radiative width (Bain & Bardsley 1972; Bennett et al. 2003; Mrugala, Spirko & Kraemer 2003; Antipov et al. 2013; Öström et al. 2016). For astrophysical environments with varying amounts of radiation and mass densities, the exact phenomenological RA rate constant would be expected to lie somewhere in-between the LTE and NLTE-ZDL rate constants reported here.

In addition to presenting two rate constants for each electronic potential curve, we also present two methods for computing the rate constants. Both methods utilize the Sturmian approach described previously (Forrey 2013, 2015). The first method calculates the rate constant using an analytic evaluation of the thermal average with respect to the Maxwell velocity distribution. The second method calculates the cross-section and performs the thermal average using numerical integration. This method is similar to conventional grid-based approaches for solving the Schrödinger equation, e.g. Numerov propagation (Cooley 1961; Johnson 1977). Grid-based methods generally need to be performed on a fine energy mesh in order to fully resolve the resonant contributions. In this case (Method 2), the size of the Sturmian basis set determines the energy density of the numerical integration grid. The contributions from narrow resonances are well resolved due to the variational nature of diagonalizing the Hamiltonian on an \mathcal{L}^2 basis set, and the remaining positive energy eigenstates represent the broad resonant and non-resonant background contribution.

For the $A^1\Pi \rightarrow X^1\Sigma^+$ transition in SiO, the RA cross-section determined from Method 2 was compared to the standard perturbation theory quantum approach (Zygelman & Dalgarno 1990; Stancil et al. 1993; Nyman et al. 2015; Öström et al. 2016). Excellent agreement was obtained for the broad features. The positions of many of the narrow resonances were also found to be in excellent agreement. The heights of the narrow resonances are not accurately determined by the grid-based approach due to the well-known breakdown of perturbation theory (Bennett et al. 2003). The Sturmian approach determines the heights of the resonances from the choice of kinetic model (LTE or NLTE). Good agreement was obtained for the NLTE-ZDL rate constant computed by the two Sturmian methods, and the rate constant is shown to be in good agreement with a semiclassical calculation at high temperatures.

2 THEORY

We describe two methods for calculating the rate constant. Both methods utilize a Sturmian representation to form a complete basis set for both the dynamics and kinetics (Forrey 2013, 2015). Following Paper I, the RA cross-section is defined by

$$\sigma_{\Lambda \rightarrow \Lambda'}(E) = \frac{\pi^2 \hbar^3}{\mu E} P_{\Lambda} \sum_{b,u} (2j_u + 1)(1 + \delta_u) \Gamma_{u \rightarrow b}^{\text{rad}} \delta(E - E_u), \quad (4)$$

where Λ and Λ' are initial and final projections of the electronic orbital angular momentum of the molecule on the internuclear axis, μ is the reduced mass of the Si+O system and E is the translational energy. Here, $b \equiv (v_b, j_b)$ and $u \equiv (v_u, j_u)$ designate vibrational and rotational quantum numbers for bound and unbound states, respectively. $\Gamma_{u \rightarrow b}^{\text{rad}}$ is the probability for a radiative transition between the unit-normalized states, and δ_u is a dimensionless parameter which may be computed within a given kinetic model to obtain the density of unbound states. The statistical factor

$$P_{\Lambda} = \frac{(2S_{\text{mol}} + 1)(2 - \delta_{0,\Lambda})}{(2L_{\text{Si}} + 1)(2S_{\text{Si}} + 1)(2L_{\text{O}} + 1)(2S_{\text{O}} + 1)} \quad (5)$$

is determined by L_{Si} , S_{Si} , L_{O} and S_{O} , the electronic orbital and spin angular momenta of the silicon and oxygen atoms, and S_{mol} is the total spin of the molecular electronic state.

The thermally averaged rate constant is defined by

$$k_{\Lambda \rightarrow \Lambda'} = \frac{1}{2\pi Q_{\text{T}}} \int_0^{\infty} E \sigma_{\Lambda \rightarrow \Lambda'}(E) e^{-E/k_{\text{B}}T} dE, \quad (6)$$

where

$$Q_{\text{T}} = \left(\frac{2\pi \hbar^2}{\mu k_{\text{B}}T} \right)^{-3/2} \quad (7)$$

is the translational partition function for temperature T and k_{B} is Boltzmann's constant. Method 1 performs the thermal average analytically by substituting (4) into (6) to obtain the rate constant

$$k_{\Lambda \rightarrow \Lambda'} = \sum_{b,u} K_u^{\text{eq}} (1 + \delta_u) \Gamma_{u \rightarrow b}^{\text{rad}} \quad (8)$$

in terms of the equilibrium constant

$$K_u^{\text{eq}} = \frac{(2j_u + 1)P_{\Lambda} \exp(-E_u/k_{\text{B}}T)}{Q_{\text{T}}}. \quad (9)$$

This method does not require computation of the cross-section. Method 2 performs the thermal average numerically using $\delta(E - E_u) = \delta_{E,E_u}/w_E$ to calculate the cross-section. Here, w_E is the equivalent quadrature weight which transforms the unit-normalized state to energy-normalization. The weights depend on

Table 1. Equilibrium bond distance R_e (Å) and dissociation energies D_e (eV) for the $X^1\Sigma^+$, $D^1\Delta$, $A^1\Pi$, $E^1\Sigma^+$ and $2^1\Pi$ states of SiO for the present MRCI+Q calculations compared to other theoretical and experimental results.

State	Method	R_e (Å)	D_e (eV)
$X^1\Sigma^+$	MRCI+Q ^a	1.5153	8.2748
	IC-MRCI ^b	1.5170	8.3277
	MRCI+Q ^c	1.5100	8.3776
	MRDCI ^d	1.5210	–
	Experiment ^e	1.5097	8.3368
	Experiment ^f	–	8.26 ± 0.13
	Experiment ^g	–	8.33 ± 0.09
	Experiment ^h	1.5100	8.18 ± 0.03
$D^1\Delta$	MRCI+Q ^a	1.7399	3.4866
	IC-MRCI ^b	1.7395	3.5359
	MRDCI ^d	1.7440	–
	Experiment ^e	1.7290	–
	Experiment ⁱ	1.7270	–
$A^1\Pi$	MRCI+Q ^a	1.6315	2.9693
	IC-MRCI ^b	1.6339	2.9629
	MRCI+Q ^c	1.6229	3.0510
	MRDCI ^d	1.6500	–
	Experiment ^e	1.6206	3.0259
	Experiment ^g	1.6200	2.87 ± 0.03
	Experiment ^j	1.6199	–
	Experiment ⁱ	1.6207	–
$E^1\Sigma^+$	MRCI+Q ^a	1.7625	1.8177
	IC-MRCI ^b	1.7415	1.7823
	MRDCI ^d	1.7550	–
	Experiment ^e	1.7398	–
	Experiment ^j	1.7399	–
$2^1\Pi$	MRCI+Q ^a	1.7650	0.5808
	IC-MRCI ^b	1.7281	0.6018
	MRDCI ^d	1.7050	–
	Experiment ⁱ	–	–

Notes. ^aMultireference configuration interaction (MRCI) and Davidson correction (+Q), aug-cc-pV6Z basis, this work.

^bInternally contracted MRCI (IC-MRCI), aug-cc-pV5Z basis (Bauschlicher 2016).

^cMRCI and Davidson correction (+Q), aug-cc-pV6Z (Shi et al. 2012).

^dMulti-reference singles-and-doubles configuration interaction (MRDCI), basis, Si (7s6p5d2f/7s6p4d1f), O(4s4p1d) (Chattopadhyaya et al. 2003).

^eExperiment (Huber & Herzberg 1979).

^fExperiment (Hildenbrand 1972).

^gExperiment (Brewer & Rosenblatt 1969).

^hExperiment (Gaydon 1968).

ⁱExperiment (Field, Lagerqvist & Renhron 1976).

^jExperiment (Lagerqvist, Renhron & Elander 1973).

j_u and may be obtained from the energy spectrum of the free Hamiltonian using the Heller derivative method (Heller 1973). The Kroencker delta function reduces equation (4) to a single sum over bound states for an energy grid comprised of unbound eigenstates of the interacting Hamiltonian. These unbound eigenstates include quasi-bound states and discretized continuum states, so both the direct process (2) and the indirect process (3) are fully accounted for

in the Sturmian formulation. Rate constants are computed by interpolating the cross-section (4) over the energy grid and numerically integrating equation (6).

The radiative width generally includes spontaneous and stimulated emission and may be written

$$\Gamma_{u \rightarrow b}^{\text{rad}} = \frac{A_{u \rightarrow b}}{1 - e^{-(E_u - E_b)/k_B T_R}} \quad (10)$$

for a pure blackbody radiation field with temperature T_R . The kinetic parameter δ_u is determined by the conditions of the gas. For a gas in LTE, the full parameter set is defined by $\delta_{u_i} = 0$. For a NLTE-ZDL gas ($T_R = 0$), the parameter set is determined by the formula (Forrey 2015)

$$1 + \delta_{u_i} = \frac{1}{1 + \tau_{u_i} \left(\sum_{j < i} A_{u_i \rightarrow u_j} + \sum_j A_{u_i \rightarrow b_j} \right)}, \quad (11)$$

where

$$\tau_{u_i}^{-1} = 2\pi |\langle u_i | V | f \rangle|^2 \quad (12)$$

is the tunnelling width and f is an energy-normalized free eigenstate with the same energy as the interacting unbound state. The Einstein A-coefficients are given by

$$A_{u_i \rightarrow b_j} = \frac{4}{3c^3} (E_{u_i} - E_{b_j})^3 S_{j u_i j b_j} |\langle u_i | M | b_j \rangle|^2 \quad (13)$$

and similarly for $A_{u_i \rightarrow u_j}$, where $S_{j u_i j b_j}$ are the appropriate line strengths (Cowan 1981; Curtis 2003) or Hönl-London factors (Watson 2008) and c is the speed of light. The electronic dipole moment is defined by

$$M = \begin{cases} \langle \psi_e | p_z | \psi'_e \rangle & \Lambda = \Lambda' \\ \frac{1}{\sqrt{2}} \langle \psi_e | p_x + i p_y | \psi'_e \rangle & \Lambda \neq \Lambda' \end{cases}, \quad (14)$$

where (p_x, p_y, p_z) are the components of the dipole operator and ψ_e is the electronic wavefunction. We note that the $\frac{1}{\sqrt{2}}$ normalization in (14) was double-counted in Paper I for the $A^1\Pi$ to $X^1\Sigma^+$ transition. The radiative and tunnelling widths have been calculated for all of the initial SiO electronic states considered in this work.

3 RESULTS

The molecular electronic structure calculations used in this work were reported on in Paper I. In that work, a multireference configuration-interaction approximation was used with the Davidson correction (MRCI +Q) and an aug-cc-pV6Z basis. The molecular orbitals were determined using the state-averaged complete active space self-consistent field (SA-CASSCF) approximation. Where necessary, we have included updated details of those molecular electronic structure calculations in this work. Recently, Bauschlicher (2016) reported similar calculations using the internally contracted multireference configuration-interaction (IC-MRCI) approximation with an aug-cc-pV5Z basis set with the molecular orbitals (MO's) obtained from dynamically weighted CASSCF calculations.

In both Paper I and Bauschlicher (2016), the MOLPRO quantum chemistry suite of molecular structure codes (Werner et al. 2015) were used. The molecular constants for several low-lying states in SiO are compared with those obtained from the work of Bauschlicher (2016) and previous theoretical and experimental work in Table 1. Good agreement is found in all cases. The largest discrepancy occurs for the bond distances for the $A^1\Pi$ and $E^1\Sigma^+$, being ~ 0.01 and 0.02 Å larger than experiment, respectively.

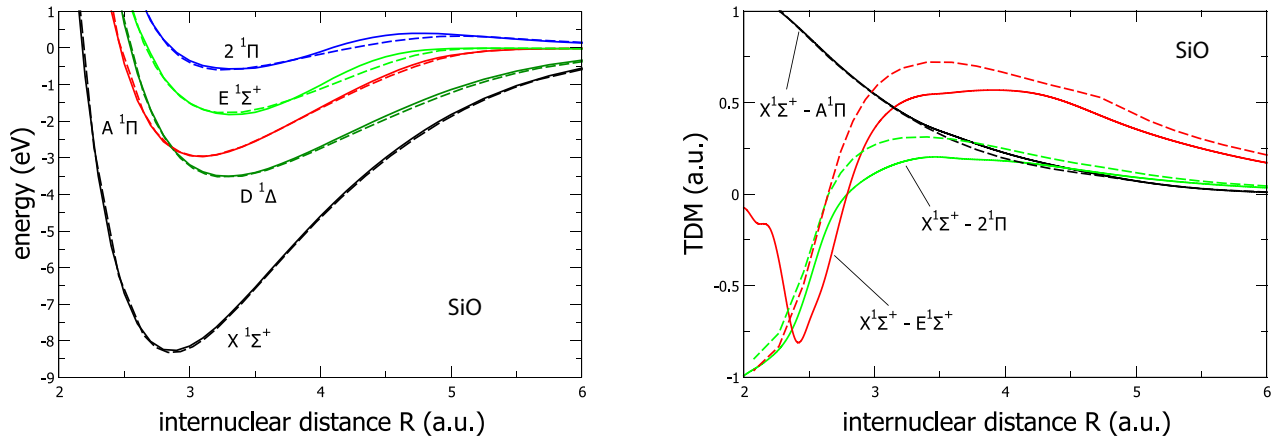


Figure 1. SiO, a comparison of the PEC's and TDM's, as a function of internuclear distance R (au), from Paper I (Forrey et al. 2016) (solid curves, MRCI + Q, AV6Z basis) with the recent molecular electronic structure calculations of Bauschlicher (2016) (dashed curves, IC-MRCI, AV5Z basis). See the text for further details.

Table 2. SiO, radiative lifetimes τ (ns) for the $v = 0, j = 0$ level of the upper electronic state.

SiO ro-vibrational transition ($v = 0, j = 0 \rightarrow v', j'$)	τ (ns) CWB ^a	τ (ns) CCD ^b	τ (ns) This work ^c
$A^1\Pi \rightarrow X^1\Sigma^+$	28.9	29.3	29.5
$E^1\Sigma \rightarrow X^1\Sigma^+$	7.1	11.0	21.7
$2^1\Pi \rightarrow X^1\Sigma^+$	14.9	29.7	90.4

Notes. ^aIC-MRCI, AV5Z basis (Bauschlicher 2016).

^bMRDCI, (4s,4p,1d) basis (Chattopadhyaya et al. 2003).

^cMRCI + Q, AV6Z basis, this work.

A comparison of the PEC's and TDM's for the two sets of calculations is illustrated in Fig. 1. The solid curves correspond to the data from Paper I and the dashed curves to the data from Bauschlicher (2016). The PEC's are in excellent agreement for the $X^1\Sigma^+$ and $A^1\Pi$ states, and the agreement is also very good for the $E^1\Sigma^+$ and $2^1\Pi$ electronic states. However, we note there is a small disagreement in the region around 4–5 au. Both calculations show a small potential barrier for the $2^1\Pi$ state. Bauschlicher (2016) reported no barrier for this state, however, the data provided to us by the author contains a small barrier of about 0.3 eV, compared to a barrier height of 0.4 eV found in this work. The TDM's show good quantitative agreement for the $X^1\Sigma^+$ to $A^1\Pi$ transition and qualitative agreement for the $X^1\Sigma^+$ to $E^1\Sigma^+$ and $X^1\Sigma^+$ to $2^1\Pi$ transitions.

Radiative lifetimes for the $A^1\Pi$, $E^1\Sigma^+$ and $2^1\Pi$ states are presented in Table 2. These lifetimes were computed by summing equation (13) over all bound levels. Excellent agreement with previous calculations (Chattopadhyaya, Chattopadhyay & Das 2003; Bauschlicher 2016) is found for the $A^1\Pi$ state, however, the agreement is poor for the other states. This may be due in small part to the differences in the potential curves noted above. The larger contribution to the discrepancy is attributable to the differences in the TDM's. The comparison given in Fig. 1 for the $E^1\Sigma \rightarrow X^1\Sigma^+$ and $2^1\Pi \rightarrow X^1\Sigma^+$ transitions shows that the TDM's from Paper I have magnitudes that are smaller than those of Bauschlicher (2016) by amounts which are consistent with the discrepancies in Table 2.

We interpolated the ab initio calculated PEC's and TDM's using cubic splines. For $R < 1.5 a_0$, the ab initio data was joined smoothly to the analytic form $a \exp(bR)$, where a and b for each state were determined by fitting. For $R > 20 a_0$, the appropriate long-range forms

were used for the separating atoms. In particular, for $\text{Si}(^3P) + \text{O}(^3P)$, this corresponds to having dispersion coefficients for the C_5/R^5 and C_6/R^6 terms. The C_6 dispersion coefficients were determined using the Slater & Kirkwood (1931) formula,

$$C_6 = \frac{3}{2} \frac{\alpha_A \alpha_B}{\sqrt{\alpha_A/N_A} + \sqrt{\alpha_B/N_B}}, \quad (15)$$

where α_A and α_B are the dipole polarisability with N_A and N_B the number of equivalent electrons of the Si and O atoms, respectively. This yielded a value for C_6 of 53.67 au for the states separating to $\text{Si}(^3P) + \text{O}(^3P)$, which is in suitable agreement with the value of 63.3 au determined from the London formula, where C_6 is determined via

$$C_6 = \frac{3}{2} \frac{\mathcal{I}_A \mathcal{I}_B}{[\mathcal{I}_A + \mathcal{I}_B]} \alpha_A \alpha_B \quad (16)$$

with \mathcal{I}_A and \mathcal{I}_B being the first ionization energies of the separated atoms A and B. The C_5 dispersion coefficients were estimated using the approach outlined in Chang (1967), which respectively gave values for the $X^1\Sigma^+$ state of 25.5 au, the $A^1\Pi$ and $E^1\Sigma^+$ states are 0.0, the $D^1\Delta$ state is 4.25 au and the $2^1\Pi$ state is -17.0 au.

In Paper I, the LTE rate constants included stimulated emission for an ideal blackbody radiation field with $T_R = T$. In this work, we neglect stimulated emission and assume that thermalization is entirely due to collisions. This yields no difference between the two LTE definitions when $T < 10^4$ K since the denominator of equation (10) is very close to unity for these temperatures. The rate constants defined here, however, are smaller than those in Paper I for $T > 10^4$ K. The results presented here also correct the double-counting error in equation (14) made in Paper I for the $A^1\Pi \rightarrow X^1\Sigma^+$ transition.

The RA rate constants for the $A^1\Pi \rightarrow X^1\Sigma^+$ contribution were computed using both Sturmian methods described above. Fig. 2 shows that the NLTE-ZDL curves for the two methods are in reasonable agreement with each other and with the semiclassical calculation. Method 1 is in near perfect agreement with the semiclassical result at high temperatures. The LTE and NLTE curves for both methods merge together at high temperature due to the diminishing importance of the resonant contribution. Discrepancies between Method 1 and Method 2 are due to the different rates of convergence of the two methods. Both methods used 500 Sturmian basis functions to obtain the rate constants shown in Fig. 2. Full convergence

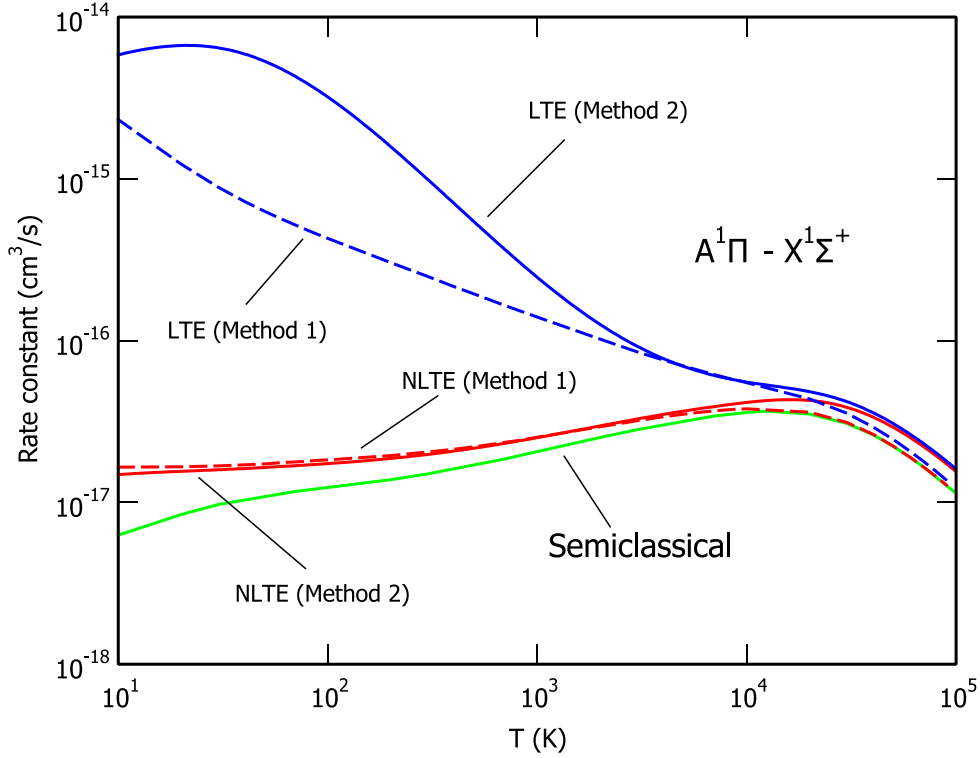


Figure 2. Radiative association rate constants ($\text{cm}^3 \text{s}^{-1}$) as a function of temperature T (K) for the $A^1\Pi \rightarrow X^1\Sigma^+$ transition in SiO. Method 1 refers to the analytical evaluation of the thermal average in equation (6) which yields equation (8). Method 2 refers to numerical integration of the thermal average in equation (6). Both methods used a Sturmian basis set of 500 functions. Full convergence was obtained for Method 1. The convergence rate for Method 2 is much slower, particularly for the LTE curve which oscillates above the converged value. It is seen that both methods converge to the semiclassical result at higher temperatures, where resonance effects are no longer important.

was achieved for Method 1. The convergence rate for Method 2, however, is much slower.

The LTE rate constant for Method 2 appears to oscillate above the converged value given by Method 1. This is due to interpolating the narrow high- j_u resonances at low energies where the energy level spacing of the Sturmian eigenvalues is relatively large. As a result, an artificial step-like structure is obtained in the cross-sections at low energies. This step goes away as the size of the basis set is increased. Fig. 3 shows our results for basis sets consisting of 500, 1000 and 1500 functions. The largest calculation for Method 2, which is computationally inefficient, has still not reached the level of convergence obtained by Method 1 using far fewer basis functions.

The LTE curve converges more slowly than the NLTE curve for Method 2 due to the enhanced importance of the resonances. This is demonstrated in Fig. 3 which shows cross-sections for elastic scattering, RA and radiative exchange (approach on the $A^1\Pi$ curve and exit on the $X^1\Sigma^+$ curve) which is negligible except at very high energies. The elastic cross-section is computed using

$$\sigma_{\text{el}}(E) = \frac{\pi^2 \hbar^2}{\mu E} P_\Lambda \sum_u (2j_u + 1)(1 + \delta_u) \tau_u^{-1} \delta(E - E_u). \quad (17)$$

As expected, the elastic cross-section is substantially larger than the RA cross-section for all energies. Tunnelling and radiative widths are computed using equations (12) and (13). These are used in equation (11) to obtain the set of kinetic parameters δ_{u_i} which are needed to describe the deviation from LTE. The kinetic parameter set is then substituted into equations (4) and (17) to obtain the NLTE-ZDL cross-sections. Fig. 3 shows that the kinetic

parameters have a dramatic effect on the resonant contribution to the cross-section. Whereas the non-resonant background contribution converges rapidly with basis set size, the resonant contribution becomes better resolved and more densely populated as the size is increased. This is particularly evident in the LTE curve which shows resonant enhancements that are typically 100 times larger than the NLTE-ZDL curve. As shown in Fig. 2, when the cross-sections are numerically integrated to obtain RA rate constants, the LTE and NLTE-ZDL curves differ by about a factor of 100 at low temperatures where the resonances are most important. The slow convergence of the LTE rate constant illustrates the difficulties associated with numerically resolving and integrating narrow resonances.

In the Sturmian theory (Forrey 2013, 2015), the heights of the resonant peaks are determined by the kinetic parameters δ_u . This is not the case for perturbation theory approaches that use a grid-based numerical method to solve the Schrödinger equation for the continuum wavefunction. Fig. 3(d) compares the RA (NLTE-ZDL) cross-section in (c) with the same cross-section obtained by a grid-based perturbative method. Clearly, the agreement between the two methods is excellent for the broad resonances and non-resonant background. As expected, the grid-based method appears to miss some of the narrow resonances in the dense region around and above 0.1 eV, and the narrow resonant peaks show variable heights. Both of these issues are related to the relative spacing of the energy grid. A fine energy-spacing is needed to resolve the narrow resonances, however, this can yield unphysically high resonant peaks such as those seen in the figure. Many of these peaks are higher than the corresponding NLTE-ZDL peaks and are examples of the so-called

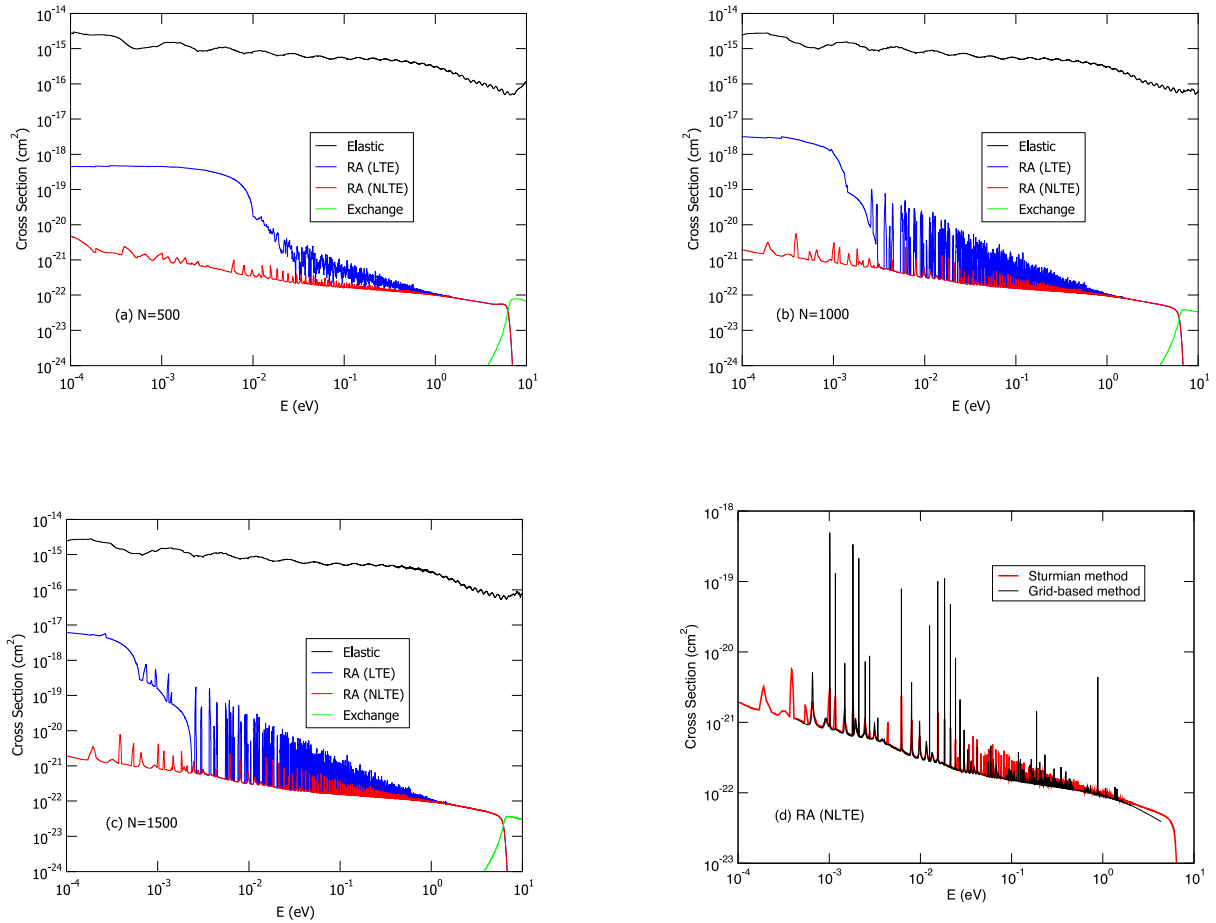


Figure 3. Cross-sections for elastic scattering, RA and radiative exchange for approach on the $A^1\Pi$ potential. The calculations used Sturmian \mathcal{L}^2 basis sets with (a) 500, (b) 1000 and (c) 1500 functions. The resonances become better resolved and more densely populated as the size of the basis set is increased. The RA (NLTE) cross-section in (c) is compared against a numerical grid-based method in (d). The peaks of the resonances are modulated by the kinetic parameters for the Sturmian \mathcal{L}^2 method but not for the quantum grid-based method.

breakdown of perturbation theory that occurs when the opacity violates unitarity (Bennett et al. 2003; Antipov et al. 2013). The set of kinetic parameters obtained from equation (11) ensures unitarity for a NLTE-ZDL gas and is equivalent to conventional methods which use radiative broadening to rescale the peaks of narrow resonances (Bain & Bardsley 1972; Bennett et al. 2003; Mrugala et al. 2003; Antipov et al. 2013).

Due to the faster convergence rate and convenience of bypassing the computation of the cross-section, we used Method 1 for the remaining calculations. The basis sets used 500 Sturmian functions with a scale factor of 75 au. All of the tunnelling and radiative widths needed to evaluate equation (11) were computed and used in equation (8) to obtain the RA rate constants. Fig. 4 shows the rate constants for $E^1\Sigma^+ \rightarrow X^1\Sigma^+$ and $A^1\Pi \rightarrow X^1\Sigma^+$ transitions. The solid curves correspond to LTE and the dashed curves to NLTE-ZDL. The $E^1\Sigma^+ \rightarrow X^1\Sigma^+$ contribution is seen to be comparable to the $A^1\Pi \rightarrow X^1\Sigma^+$ contribution. In both cases, the LTE and NLTE-ZDL curves are well-separated at low temperature and gradually approach each other as the temperature is increased due to the diminishing importance of the resonances.

Fig. 5 shows RA rate constants for the $2^1\Pi \rightarrow X^1\Sigma^+$ and the $3^1\Pi \rightarrow X^1\Sigma^+$ transitions. Qualitatively similar behaviour is observed for the $2^1\Pi$ and $A^1\Pi$ LTE curves. Two NLTE-ZDL curves are shown for the $2^1\Pi$ state. The dashed curve corresponds to calcu-

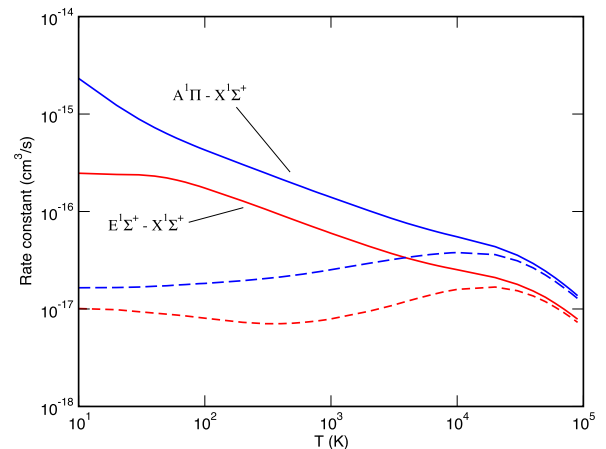


Figure 4. Radiative association rate constants for the $E^1\Sigma^+ \rightarrow X^1\Sigma^+$ and $A^1\Pi \rightarrow X^1\Sigma^+$ transitions in SiO. Solid curves correspond to LTE and dashed curves to NLTE.

lations which include tunnelling widths (12) for the $2^1\Pi$ potential. This curve shows a strong threshold effect due to a barrier in the potential curve (Chattopadhyaya et al. 2003; Forrey et al. 2016), which prevents low energy collisions from approaching close separations

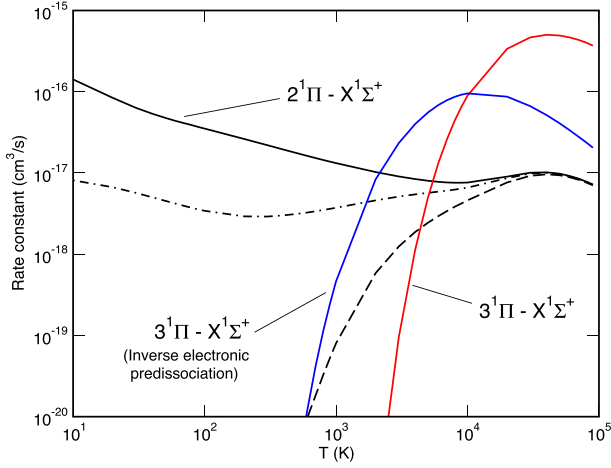


Figure 5. Radiative association rate constants for $2^1\Pi \rightarrow X^1\Sigma^+$ and $3^1\Pi \rightarrow X^1\Sigma^+$ transitions in SiO. Solid curves correspond to LTE and broken curves to NLTE-ZDL. The dashed broken curve, which uses only the tunnelling widths for the $2^1\Pi$ potential, shows a threshold due to a barrier in the potential. The dot-dashed curve includes tunnelling widths from the $A^1\Pi$ potential, which removes the threshold for the $2^1\Pi$ rate constant. The rate constants for the $3^1\Pi$ state have thresholds that are due to the asymptotic shift in the potential. The red curve corresponds to approach on the $3^1\Pi$ state. The blue curve corresponds to a radiation-less transition from the $A^1\Pi$ state to an intermediate bound level of the $3^1\Pi$ state prior to radiative decay to the $X^1\Sigma^+$ state.

where the TDM is largest. The $2^1\Pi$ potential of Bauschlicher (2016) has a somewhat smaller barrier suggesting some uncertainty in the rate constant given by the dashed curve. The dot-dashed curve corresponds to calculations which include tunnelling widths (12) for both the $2^1\Pi$ and the $A^1\Pi$ potentials. Since the $A^1\Pi$ potential has no barrier, the threshold is removed and the NLTE-ZDL rate constant appears more in-line with those presented in Fig. 4.

Fig. 5 also shows two RA contributions from the $3^1\Pi$ state. The $3^1\Pi$ state separates at long internuclear distance to $\text{Si}(^1D)+\text{O}(^1D)$, which is shifted from the $\text{Si}(^3P)+\text{O}(^3P)$ asymptote by 2.7 eV. This produces a threshold for RA via the $3^1\Pi$ state (red curve) which is at a sufficiently high energy such that resonances do not make a substantial contribution, and that the LTE and NLTE-ZDL rate constants are virtually identical. It should be noted that the $3^1\Pi$ state also allows RA to take place through inverse electronic predissociation. In this process, bound ro-vibrational levels of the $3^1\Pi$ state are populated by approach on the $A^1\Pi$ state, characterized by the tunnelling widths (12). Subsequently, the bound levels of the $3^1\Pi$ state can decay to the $X^1\Sigma^+$ in a similar manner to the quasi-bound rotational states which contribute to RA through inverse rotational predissociation. When the translational energy of the approaching atoms is large enough to match the energy of the bound levels of the $3^1\Pi$ state, the rate constant is non-zero and rises rapidly (blue curve). It is noteworthy that the bottom of the potential well for the $3^1\Pi$ state has an energy which is approximately the same as the energy of the potential barrier for the $2^1\Pi$ state. This causes the threshold for the $3^1\Pi$ inverse electronic predissociation curve to be at about the same temperature as the threshold for the $2^1\Pi$ NLTE-ZDL curve. The relatively large maximum for the red $3^1\Pi$ curve is due to large energy differences involved in the radiative transitions and the replacement of $P_{\Pi} = 2/81$ with $P_{\Pi} = 2/25$ due to the different atomic asymptotes. The blue $3^1\Pi$ curve does not undergo this statistical replacement since the atoms approach each other on the $A^1\Pi$ state.

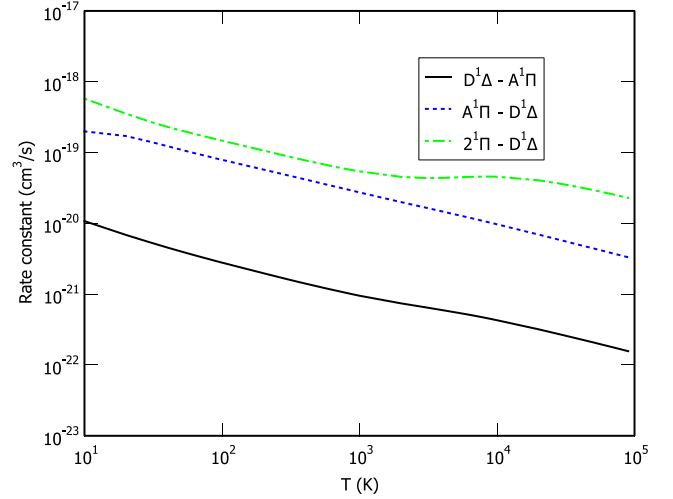


Figure 6. Radiative association rate constants for transitions in SiO. The dashed line (blue) is $A^1\Pi \rightarrow D^1\Delta$, dot dashed line (green) $2^1\Pi \rightarrow D^1\Delta$ and the solid line (black) is $D^1\Delta \rightarrow A^1\Pi$

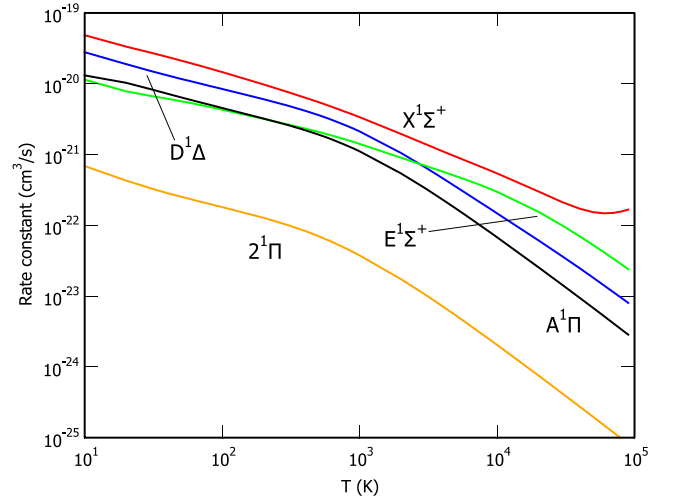


Figure 7. Radiative association rate constants due to permanent dipoles for $X^1\Sigma^+$, $D^1\Delta$, $E^1\Sigma^+$, $A^1\Pi$ and $2^1\Pi$ in SiO.

Fig. 6 shows RA rate constants for $A^1\Pi \rightarrow D^1\Delta$, $2^1\Pi \rightarrow D^1\Delta$ and $D^1\Delta \rightarrow A^1\Pi$ transitions. These rate constants are smaller than those which lead to the formation of bound states for the $X^1\Sigma^+$ potential. The $A^1\Pi$, $D^1\Delta$ and $E^1\Sigma^+$ potentials also support bound states, however, the dissociation energies of these electronic states are less than that of the $X^1\Sigma^+$. Consequently, the $(\Delta E)^3$ factor in equation (13) is not as large and the RA rate constants are smaller. The three curves shown in Fig. 6 are the largest among all transitions which do not include $X^1\Sigma^+$ bound states. These curves represent the LTE rate constants; the NLTE-ZDL rate constants have the usual fall-off behaviour with decreasing temperature and are not shown. RA rate constants for $D^1\Delta$ to $E^1\Sigma^+$ and $X^1\Sigma^+$ to $A^1\Pi$, $D^1\Delta$ and $E^1\Sigma^+$ were computed and found to be smaller than $10^{-25} \text{ cm}^3 \text{ s}^{-1}$.

Fig. 7 shows permanent dipole contributions for the $X^1\Sigma^+$, $E^1\Sigma^+$, $A^1\Pi$, $2^1\Pi$ and $D^1\Delta$ states. Again, only the LTE rate constants are shown due to the relatively small values of the NLTE-ZDL rate constants at low temperatures. The LTE rate constants are comparable in magnitude to the transition dipole contributions shown in Fig. 6.

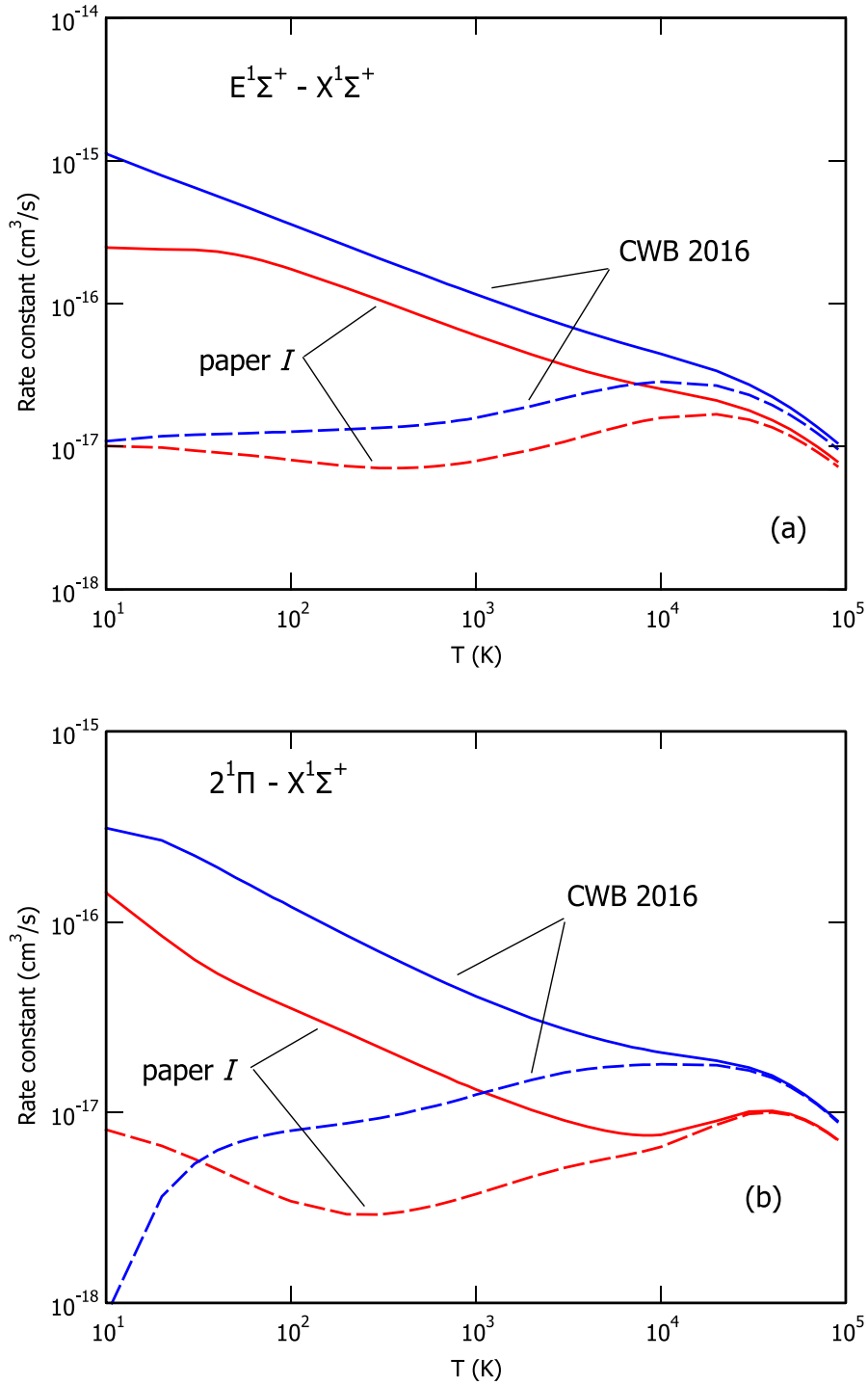


Figure 8. A comparison of the rate constants using the molecular data for PEC's and TDM's from Paper I (Forrey et al. 2016, red curves) and that from Bauschlicher (2016) (blue curves). (a) $E^1\Sigma^+ \rightarrow X^1\Sigma^+$ and (b) $2^1\Pi \rightarrow X^1\Sigma^+$ transitions in SiO. Solid lines in both cases correspond to LTE and dashed lines to NLTE-ZDL.

Having considered all possible RA contributions, it is clear that formation of SiO is dominated by the $A^1\Pi$, $E^1\Sigma^+$ and $2^1\Pi$ states at low temperatures and by the $3^1\Pi$ state at high temperatures. In order to estimate the uncertainty in the RA rate constants for these states, we compare results using the molecular data of Bauschlicher (2016) with those obtained using data from Paper I. As expected from the comparisons shown in Fig. 1, the rate constants for the $A^1\Pi$ to $X^1\Sigma^+$ transition were virtually identical, so the comparison

is not shown. The $E^1\Sigma^+$ to $X^1\Sigma^+$ and $2^1\Pi$ to $X^1\Sigma^+$ comparisons are shown in Fig. 8. Consistent with the lifetimes presented in Table 2, the RA rate constants calculated with the molecular data of Bauschlicher (2016) tend to be about 2–3 times larger than those obtained using the molecular data from Paper I. It should be noted that the appropriate long-range forms for each state were included for the molecular curves from Paper I but not for the CWB potentials. The rate constants are found to be sensitive to the long-range for

Table 3. Parameters for the analytic formula (19) used to fit the SiO rate coefficients as a function of temperature T (K) over the range 10 – 10,000 K.

Fitting parameter	$A^1\Pi \rightarrow X^1\Sigma^+$		$E^1\Sigma \rightarrow X^1\Sigma^+$		$2^1\Pi \rightarrow X^1\Sigma^+$	
	LTE	NLTE-ZDL	LTE	NLTE-ZDL	LTE	NLTE-ZDL
a	2.08233	0.222128	0.816526	0.0846568	0.244134	0.0360735
b	0.420491	−0.161335	0.373286	−0.0982334	0.488114	−0.168372
c_1	481.186	5.71969	879.858	7.91451	−174.301	9.10961
c_2	0	0	−8.44818	−1191.94	−695.992	−237.498
c_3	0	0	−21.8148	273 212	150 707	11 728.5
d_1	1.37764	14.09	78.2256	18.4612	45.4479	15.4816
d_2	0	0	0.3277	830.387	388.013	536.223
d_3	0	0	3.05515	19 999.8	18243.8	12 844.6

$T < 100$ K (see supplementary material). The enhanced sensitivity of the NLTE-ZDL rate constant in Fig. 8(b) is due to the barrier in the $2^1\Pi$ potential and the coupling to the $A^1\Pi$ state.

4 SUMMARY AND CONCLUSIONS

Two methods were used to compute RA rate constants for $A^1\Pi$ to $X^1\Sigma^+$ transitions. Both methods employed Sturmian basis sets to represent the bound and unbound ro-vibrational states. Results for the two methods are found to be in good agreement, however, Method 1 converges more rapidly and does not require calculation of the cross-section. This method was subsequently used to calculate LTE and NLTE-ZDL rate constants for the low-lying electronic states of SiO. The LTE rate constants assume that all unbound states, including long-lived quasi-bound states, are populated by a Boltzmann equilibrium distribution. The NLTE-ZDL rate constants refer to a dilute gas at $T_R = 0$, which have no excitation mechanisms. More general NLTE environments which have some collisional and/or radiative excitation capability would presumably have rate coefficients which lie somewhere in-between the NLTE-ZDL and LTE curves.

In light of the expectation that the true formation rate constant lies in-between the LTE and NLTE-ZDL values, it is tempting to provide a formula which interpolates between the two limits. This approach has been adopted previously (Lepp & Shull 1983; Martin, Schwarz & Mandy 1996; Glover & Abel 2008) for interpolating collision-induced dissociation rates between low and high density.

However, it should be noted, that there are two distinct ways to achieve the LTE results given here. The first assumes that the density is large enough that the quasi-bound states may be populated by three-body collisions. In this case, the total recombination rate constant

$$k_r = k_r^{(2)} + k_r^{(3)}n \quad (18)$$

would likely be dominated by the TBR contribution $k_r^{(3)}$. Therefore, the LTE RA rate constant $k_r^{(2)}$ may be used to estimate the TBR rate at the critical density n_{cr} , and it is possible that an interpolating scheme between low and high densities would be useful. The second way to achieve the LTE RA rate constant is to assume a pure blackbody radiation field with $T_R = T$ (Forrey 2015). Realistic radiation fields are generally less intense than a pure blackbody field, so a formula for interpolating between $T_R = 0$ and $T_R = T$ would need to account for the dilution. See Ramaker & Peek (1979) for an example where such an approach would be useful.

A simpler approach would be to use both the LTE and NLTE-ZDL rate constants in separate calculations to provide theoretical error bars in any model which depends on the SiO formation rate. To facilitate this approach, we provide analytic fitting functions

(Novotný et al. 2013; Vissapragada et al. 2016) for both LTE and NLTE-ZDL rate constants using the form

$$k_r = \left[a(400/T)^b + T^{-3/2} \sum_{i=1}^3 c_i \exp(-d_i/T) \right] \times 10^{-16} \text{ cm}^3 \text{ s}^{-1}, \quad (19)$$

where the parameters are given in Table 3. This formula provides a fit to the rates to better than 10 per cent over the temperature range 10–10 000 K. A plot which compares the fitted rates with the calculated rates is included in the supplementary material. Also included in the supplementary data are the molecular data used to compute the rates. The primary source of error in the calculations is due to the TDM uncertainties (see Fig. 1b) which yield rate constants that differ by 2–3 times over the temperature range considered.

ACKNOWLEDGEMENTS

MC and RCF acknowledge support from NSF grant no. PHY-1503615. PCS acknowledges support from NASA grant no. NNX16AF09G. BMMcL acknowledges support from the ITAMP visitor's program, Queen's University Belfast for the award of a Visiting Research Fellowship (VRF) and the hospitality of the University of Georgia during recent research visits. ITAMP is supported in part by a grant from the NSF to the Smithsonian Astrophysical Observatory and Harvard University. We would like to thank Dr. Charles W. Bauschlicher from NASA Ames, for sending us his data in numerical format. Grants of computational time at the National Energy Research Scientific Computing Center (NERSC) in Berkeley, CA, USA and at the High Performance Computing Center Stuttgart (HLRS) at the University of Stuttgart, Stuttgart, Germany are gratefully acknowledged. This research made use of the NASA Astrophysics Data System.

REFERENCES

- Andreaazza C. M., Singh P. D., Sanzovo G. C., 1995, *ApJ*, 451, 889
- Antipov S. V., Gustafsson M., Nyman G., 2013, *MNRAS*, 430, 946
- Bain R. A., Bardsley J. N., 1972, *J. Phys. B: At. Mol. Phys.*, 5, 277
- Bates D. R., 1951, *MNRAS*, 111, 303
- Bauschlicher C. W., Jr, 2016, *Chem. Phys. Lett.*, 658, 76
- Bennett O. J., Dickinson A. S., Leininger T., Gad  a X., 2003, *MNRAS*, 341, 361
- Brewer K., Rosenblatt G. M., 1969, in Eyring L., ed., Vol. 2, *Advances in High-Temperature Chemistry*. Academic Press, New York, USA, p. 1
- Chang T. Y., 1967, *Rev. Mod. Phys.*, 39, 911
- Chattopadhyaya S., Chattopadhyay A., Das K. K., 2003, *J. Phys. Chem. A*, 107, 148
- Cherchneff I., 2006, *A&A*, 456, 1001

- Cherchneff I., 2012, *A&A*, 545, A12
- Cooley J. W., 1961, *Math. Comput.*, 15, 363
- Cowan R. D., 1981, *The Theory of Atomic Structure and Spectra*. Univ. California Press, Berkeley, California, USA
- Curtis L. J., 2003, *Atomic Structure and Lifetimes: A conceptual Approach*. Cambridge Univ. Press, Cambridge, UK
- Dalgarno A., Du M. L., You J. H., 1990, *ApJ*, 349, 675
- Field R. W., Lagerqvist A., Renhron I., 1976, *Phys. Scripta*, 14, 298
- Forrey R. C., 2013, *Phys. Rev. A*, 88, 052709
- Forrey R. C., 2015, *J. Chem. Phys.*, 143, 024101
- Forrey R. C., Babb J. F., Stancil P. C., McLaughlin B. M., 2016, *J. Phys. B: At. Mol. Opt. Phys.*, 48
- Franz J., Gustafsson M., Nyman G., 2011, *MNRAS*, 414, 3547
- Gaydon A. G., 1968, *Dissociation energies and Spectra of Diatomic Molecules*. Chapman & Hall, London, UK
- Gearhart R., Wheeler J., Swartz D., 1999, *ApJ*, 510, 944
- Glover S. C. O., Abel T., 2008, *MNRAS*, 388, 1627
- Heller E. J., 1973, PhD thesis, Harvard University
- Hildenbrand D. L., 1972, *H. Temp. Sci.*, 4, 244
- Huber K. P., Herzberg G., 1979, *Molecular Spectra and Molecular Structure IV: Constants of Diatomic Molecules*. Van Nostrand-Reinhold, Princeton, New Jersey, USA
- Johnson B. R., 1977, *J. Chem. Phys.*, 67, 4086
- Lagerqvist A., Renhron I., Elander N., 1973, *J. Molec. Spectrosc.*, 46, 285
- Lepp S., Shull J. M., 1983, *ApJ*, 270, 578
- Lepp S., Dalgarno A., McCray R., 1990, *ApJ*, 358, 262
- Li X., Millar T. J. C. W., Heays A. N., van Dishoeck E. F., 2014, *A&A*, 568, A111
- Li X., Millar T. J., Heays A. N. C. W., van Dishoeck E. F., Cherchneff I., 2016, *A&A*, 588, A4
- Liu W., Dalgarno A., 1996, *ApJ*, 471, 480
- Marassi S., Schneider R., Limongi M., Chieffi A., Bocchio M., Bianchi S., 2015, *MNRAS*, 454, 4250
- Martin P. G., Schwarz D. H., Mandy M. E., 1996, *ApJ*, 461, 265
- Mrugala F., Spirko V., Kraemer W. P., 2003, *J. Chem. Phys.*, 118, 10547
- Novotný O. et al., 2013, *ApJ*, 777, 54
- Nyman G., Gustafsson M., Antipov S. V., 2015, *Int. Rev. Phys. Chem.*, 34, 385
- Öström J., Bezrukov D., Nyman G., Gustafsson M., 2016, *J. Chem. Phys.*, 144, 044302
- Ramaker D. E., Peek J. M., 1979, *J. Chem. Phys.*, 71, 1844
- Rawlings J. M. C., Williams D. A., 1989, *MNRAS*, 240, 729
- Shi D., Li W., Sun J., Zhu Z., 2012, *Spectrochim. Acta Part A*, 87, 96
- Slater J. C., Kirkwood J. G., 1931, *Phys. Rev.*, 37, 682
- Stancil P. C., Babb J. F., Dalgarno A., 1993, *ApJ*, 414, 672
- Vissapragada S., Buzard C. F., Miller K. A., O'Connor A. P., de Ruette N., Urbain X., Savin D. W., 2016, *ApJ*, 832, 31
- Watson J. K. G., 2008, *J. Molec. Spectrosc.*, 253, 5
- Werner H. J., Knowles P. J., Manby F. R., Schütz M., 2015, *MOLPRO*, available at: <http://www.molpro.net>
- Willacy K., Cherchneff I., 1998, *A&A*, 330, 676
- Zygelman B., Dalgarno A., 1990, *ApJ*, 365, 239

SUPPORTING INFORMATION

Supplementary data are available at *MNRAS* online.

supp.pdf

Please note: Oxford University Press is not responsible for the content or functionality of any supporting materials supplied by the authors. Any queries (other than missing material) should be directed to the corresponding author for the article.

This paper has been typeset from a \LaTeX file prepared by the author.